

# Universal scaling of extreme vorticity regions and the structure of the vortex lines representation\*

D.S. Agafontsev<sup>(a),(b)</sup>, E.A. Kuznetsov<sup>(b),(c)</sup> and A.A. Mailybaev<sup>(d)</sup>

<sup>(a)</sup> *P. P. Shirshov Institute of Oceanology, Moscow, Russia*

<sup>(b)</sup> *Novosibirsk State University, Novosibirsk, Russia*

<sup>(c)</sup> *P.N. Lebedev Physical Institute, Moscow, Russia*

<sup>(d)</sup> *Instituto Nacional de Matemática Pura e Aplicada – IMPA, Rio de Janeiro, Brazil*

The incompressible three-dimensional ideal flows develop very thin pancake-like regions of increasing vorticity, which evolve with the scaling  $\omega_{\max} \propto \ell^{-2/3}$  between the vorticity maximum and the pancake thickness. We study this process from the point of view of the vortex lines representation (VLR), which describes the associated dynamics of the compressible “flow” of continuously distributed vortex lines. Based on numerical simulations of the VLR equations in adaptive anisotropic grids of up to  $1536^3$  nodes for two initial flows, we show that the vorticity growth is connected with the compressibility of the vortex lines and find the link between the scaling law  $\omega_{\max} \propto \ell^{-2/3}$  and the geometric properties of the VLR.

PACS numbers: 47.27.Cn, 47.27.De, 47.27.ek

## I. INTRODUCTION

The incompressible 3D Euler equations develop high-vorticity regions with increasing time. The mechanism of vorticity growth was addressed in numerous studies because of its relation to a possible finite-time blowup and subsequent transition to turbulence. Several analytical blowup and no-blowup criteria were established; see the reviews in [1] and [2]. In parallel, a large effort was made with numerical analysis. One of the early numerical studies [3] examined evolution of periodic flows in  $256^3$  grids for random initial conditions and in  $864^3$  grids for the symmetric Taylor–Green vortex. In all cases, the maximum of

---

\*dmitrij@itp.ac.ru

vorticity was growing nearly exponentially with time, and the regions of high vorticity were confined within pancake-like structures (thin vortex sheets). Since the tendency toward a vortex sheet should suppress three-dimensionality of the flow, formation of a finite-time singularity is not expected as the dynamics of the 2D Euler equations is known to be regular; see [4] and the related discussion in [5, 6]. Thus, further numerical studies were mainly concentrated on carefully designed initial conditions providing enhanced vorticity growth; we refer to [2] and [7] for a brief review, as well as to [8–10] for examples of recent numerical works. It is fair to say that, despite these efforts, the existence of blowup (unless it is triggered by physical boundary [11]) remains a highly controversial question.

In our previous studies [7, 12, 13] we returned to the problem of vorticity growth from generic large-scale initial conditions. We carried out several simulations in anisotropic grids with up to  $2048^3$  total number of nodes and observed in details evolution of high-vorticity regions. We confirmed that these regions represent pancake-like structures and found that the flow near the pancake is described locally by the novel exact self-similar solution of the Euler equations combining a shear flow with an asymmetric straining flow. The maximum vorticity growth  $\omega_{\max}(t) \propto e^{\beta_2 t}$  and the pancake compression in the transversal direction  $l(t) \propto e^{-\beta_1 t}$  are characterized by significantly different exponents  $\beta_2/\beta_1 \approx 2/3$ , leading to the Kolmogorov-type scaling law

$$\omega_{\max}(t) \propto l(t)^{-2/3} \tag{1}$$

during the pancake evolution. The pancake structures emerge in increasing number with time. These structures provide the leading contribution to the energy spectrum, where, for some initial flows [7, 12], we observed the gradual formation of the Kolmogorov spectrum,  $E(k) \propto k^{-5/3}$ , in a fully inviscid flow.

In the present paper we study the pancake vorticity structures from the new perspective of the vortex lines representation (VLR). The underlying idea of this representation is that the transformation from the Eulerian coordinates of the fluid to the Lagrangian markers of the vortex lines – the VLR – is compressible [14] and its Jacobian may take arbitrary values, despite incompressibility of the fluid. Then, by analogy with gas dynamics [15], the development of intense vorticity may be explained by the vanishing Jacobian of the VLR [16–18]. We developed a numerical method for the Euler equations in terms of the VLR, and performed high-resolution simulations for two initial flows. With these simula-

tions, we confirmed that the regions of high vorticity indeed correspond to the decreasing VLR Jacobian. Combining the VLR with the pancake model solution of [13], we link the emergence of the scaling law (1) with the geometrical properties of the VLR. We argue that the discussed approach may be applicable for a larger class of the so-called “frozen-in-fluid” fields advected by incompressible fluids, for instance, the magnetic field in MHD [19].

We start with a general introduction to the frozen-in-fluid fields and the VLR in Section II. Detailed description of our numerical methods is given in Section III. Based on numerical simulations, we examine correspondence between the high-vorticity and the low-Jacobian structures in Section IV. In Section V we write the VLR for the pancake model solution of [13], and in Section VI we analyze the VLR mapping near the pancake structure, linking the scaling law (1) with the geometrical properties of the VLR. We finish with the Conclusions. Appendix A contains initial conditions and Appendix B describes results for the second simulation.

## II. VORTEX LINES REPRESENTATION

For the 3D Euler equations

$$\frac{\partial \mathbf{v}}{\partial t} + (\mathbf{v} \cdot \nabla) \mathbf{v} = -\nabla p, \quad \text{div } \mathbf{v} = 0, \quad (2)$$

describing dynamics of ideal incompressible fluid of unit density, the vorticity  $\boldsymbol{\omega} = \nabla \times \mathbf{v}$  satisfies the Helmholtz vorticity equation,

$$\frac{\partial \boldsymbol{\omega}}{\partial t} = \nabla \times (\mathbf{v} \times \boldsymbol{\omega}). \quad (3)$$

This equation shows that vorticity represents an example a frozen-in-fluid divergence-free field. Indeed, with the divergence-free conditions,  $\text{div } \mathbf{v} = 0$  and  $\text{div } \boldsymbol{\omega} = 0$ , Eq. (3) can be rewritten as

$$\frac{d\boldsymbol{\omega}}{dt} = (\boldsymbol{\omega} \cdot \nabla) \mathbf{v}, \quad (4)$$

where  $d/dt = \partial/\partial t + \mathbf{v} \cdot \nabla$  is the material time derivative. It has the same form as the evolution equation for an infinitesimal vector  $\delta \mathbf{x}$  between the two fluid particles,

$$\frac{d\delta \mathbf{x}}{dt} = \delta \mathbf{v} = (\delta \mathbf{x} \cdot \nabla) \mathbf{v}. \quad (5)$$

This means that the vector  $\delta \mathbf{x}$  initially parallel to  $\boldsymbol{\omega}$  retains this property at later times, i.e., fluid particles belonging initially to the same vortex line (a line tangent to  $\boldsymbol{\omega}$  at each point)

move together with this line. One can say that the vortex lines are “frozen” into the fluid during its motion. Other classical examples of frozen-in-fluid fields are the magnetic field in the magnetohydrodynamics [19] and the divorticity field for 2D Euler hydrodynamics [20].

In the present paper we focus on the behavior of vortex lines. As follows from Eq. (3), a vortex line can only be changed by the velocity component  $\mathbf{v}_n$  perpendicular to  $\boldsymbol{\omega}$ . To clarify this property, we introduce a new type of trajectories given by the modified equations of motion

$$\frac{d\mathbf{x}}{dt} = \mathbf{v}_n(\mathbf{x}, t) \quad (6)$$

with the initial condition

$$\mathbf{x}|_{t=0} = \mathbf{a}. \quad (7)$$

A solution  $\mathbf{x} = \mathbf{x}(\mathbf{a}, t)$  may be seen as describing the motion of vortex lines. In terms of this solution, Eq. (3) admits explicit integration in the form [21, 22]

$$\boldsymbol{\omega}(\mathbf{x}, t) = \frac{\widehat{\mathbf{J}}\boldsymbol{\omega}_0(\mathbf{a})}{J}, \quad \widehat{\mathbf{J}}(\mathbf{a}, t) = \left[ \frac{\partial x_i}{\partial a_j} \right], \quad J = \det \widehat{\mathbf{J}}, \quad (8)$$

where  $\boldsymbol{\omega}_0(\mathbf{a})$  is the initial vorticity at  $t = 0$  (analogous to the Cauchy invariant) and  $\widehat{\mathbf{J}}$  is the Jacobi matrix of the mapping  $\mathbf{x} = \mathbf{x}(\mathbf{a}, t)$ . Due to Eq. (7), the initial Jacobian determinant is unity,  $J|_{t=0} = 1$ .

The inverse of the Jacobian,  $n = 1/J$ , has the meaning of instant density of fluid particles with Lagrangian markers  $\mathbf{a}$ , as  $\int d^3\mathbf{x}/J = \int d^3\mathbf{a}$ , and satisfies the continuity equation,

$$\frac{\partial n}{\partial t} + \text{div}(n\mathbf{v}_n) = 0.$$

Generally,  $\text{div} \mathbf{v}_n \neq 0$ , and the density  $n$  is not preserved, emphasizing the compressible character of the mapping  $\mathbf{x} = \mathbf{x}(\mathbf{a}, t)$ , despite the flow incompressibility and the divergence-free feature of the field  $\boldsymbol{\omega}$  itself. In a generic case, a sustained growth of vorticity should be related to simultaneous decrease of the Jacobian in the denominator of Eq. (8), i.e., growth of the density  $n$ , what may be seen as formation of high density of vortex lines.

Equations (6)–(8) together with the relation  $\boldsymbol{\omega} = \nabla \times \mathbf{v}$  are called the *vortex lines representation* (VLR), and form a complete system equivalent to the Euler equations [14]. However, this system is written in the mixed Eulerian ( $\mathbf{x}$ -space) and Lagrangian ( $\mathbf{a}$ -space) variables. For numerical study, we now rewrite it using the Eulerian variables.

Let  $\mathbf{a} = \mathbf{a}(\mathbf{x}, t)$  be the mapping inverse to  $\mathbf{x} = \mathbf{x}(\mathbf{a}, t)$ . As follows from (6)–(7), this mapping obeys

$$\frac{\partial \mathbf{a}}{\partial t} + (\mathbf{v}_n \cdot \nabla) \mathbf{a} = 0. \quad (9)$$

Equation (8) can be rewritten in the form [22]

$$\omega_i(\mathbf{x}, t) = \frac{1}{2} \varepsilon_{ijk} \varepsilon_{\alpha\beta\gamma} \omega_{0\alpha}(\mathbf{a}) \frac{\partial a_\beta}{\partial x_j} \frac{\partial a_\gamma}{\partial x_k}, \quad (10)$$

where  $\boldsymbol{\omega}_0(\mathbf{a}) = (\omega_{01}, \omega_{02}, \omega_{03})$  is the initial vorticity at  $t = 0$  and  $\varepsilon_{ijk}$  is the Levi-Civita symbol; summation is assumed with respect to repeated indexes. The two equations (9) and (10) together with the relations

$$\mathbf{v} = \text{rot}^{-1} \boldsymbol{\omega} = -\Delta^{-1} (\nabla \times \boldsymbol{\omega}), \quad \mathbf{v}_n = \mathbf{v} - \frac{(\mathbf{v} \cdot \boldsymbol{\omega})}{\omega^2} \boldsymbol{\omega} \quad (11)$$

for the velocity and the normal velocity represent complete VLR system of equations written in the Eulerian coordinates  $(\mathbf{x}, t)$ .

### III. NUMERICAL METHODS

To examine the process of pancake development from the VLR point of view, we solve the system (9)–(11) numerically in the box  $\mathbf{x} = (x_1, x_2, x_3) \in [-\pi, \pi]^3$  with periodic boundary conditions. We use Runge–Kutta forth-order pseudo-spectral method and start from the initial conditions given by the mapping  $\mathbf{a}(\mathbf{x}, 0) = \mathbf{x}$  and the initial vorticity  $\boldsymbol{\omega}_0(\mathbf{x})$ . In our implementation, we use the VLR equations rewritten for the periodic mapping

$$\mathbf{b}(\mathbf{x}, t) = \mathbf{a}(\mathbf{x}, t) - \mathbf{x}, \quad (12)$$

because the original mapping  $\mathbf{a}(\mathbf{x}, t)$  is not periodic. The inverse of the curl operator in Eq. (11), as well as all spatial derivatives, are calculated in the Fourier space, see, e.g., [7]. To avoid the so-called bottle-neck instability, at each time step we perform filtering in the Fourier space with the cut-off function [23]

$$\rho(\mathbf{k}) = \exp \left( -36 \sum_j (k_j / K_{\max}^{(j)})^{36} \right), \quad (13)$$

which cuts approximately 20% of modes at the edges of the spectral band in each direction. Here  $K_{\max}^{(j)} = N_j/2$  are the maximal wavenumbers and  $N_j$  are numbers of nodes along

directions  $j = 1, 2, 3$ . The initial vorticity is given analytically, which allows for an exact calculation of  $\boldsymbol{\omega}_0(\mathbf{a})$  for a “shifted”  $\mathbf{a}$ -grid in Eq. (10).

We use adaptive anisotropic rectangular grid proposed in [7], which is uniform for each direction and adapted independently along each spatial coordinate. The idea for the adaptation comes from the standard dealiasing rule. At early times, the Fourier spectrum of the solution is concentrated at low harmonics, while higher harmonics contain numerical noise. We track the “signal-noise” boundary [7] until it reaches  $K_{\max}^{(j)}/2$  for any of the three directions  $j = 1, 2, 3$ , and then refine the grid along the corresponding direction. This rule is optimized for cubic nonlinearity of the VLR equations (9)–(11), while for the direct Euler simulations with quadratic nonlinearity we used  $2K_{\max}^{(j)}/3$ , see [7, 12, 13]. Transition to a refined grid is performed with the Fourier interpolation, which has an error comparable with the round-off. While the simulation is running in this way, the aliasing error is avoided and the cut-off function (13) affects only harmonics containing numerical noise.

We start simulations in cubic grid  $192^3$ . When the total number of nodes  $N_1N_2N_3$  reaches  $1536^3$ , we continue with the fixed grid. As a stopping criterion, at  $K_{\max}^{(j)}/2$  we compare the Fourier spectrum of the mapping (12) along each spatial direction with  $10^{-13}$  times its maximum value, see [7] where the analogous procedure was implemented. After the grid is fixed, aliasing in Eq. (10) becomes significant, but it contributes mainly to harmonics close to the edges of the spectral band. To diminish this contribution, we optimize the shape of the cut-off function (13) dynamically for the vorticity function, which features a narrower spectrum. This further improves efficiency of our method.

We use Runge–Kutta fourth-order method with adaptive time stepping implemented through the CFL stability criterion with the Courant number 0.5. Our numerical scheme conserves the total energy  $E = (1/2) \int \mathbf{v}^2 d^3\mathbf{x}$  and the helicity  $\Omega = \int (\mathbf{v} \cdot \boldsymbol{\omega}) d^3\mathbf{x}$  with a relative error smaller than  $10^{-11}$ . We compared results of the scheme for the vorticity field  $\boldsymbol{\omega}(\mathbf{x})$  using different Fourier filtering functions  $\rho(\mathbf{k})$  (see e.g. [23]) and different limitations for the total number of nodes  $N_1N_2N_3$ , and found these results practically converging.

We tested several large-scale initial conditions in the form of a superposition of the shear flow  $\boldsymbol{\omega}_0 = (\sin x_3, \cos x_3, 0)$  and a random truncated (up to second harmonics) periodic perturbation. We only considered initial flows without null points,  $\|\boldsymbol{\omega}_0(\mathbf{a})\| \neq 0$ . This is done because in Eq. (11) the VLR scheme has a topological singularity at a null point of vorticity, see e.g. [22], and we prefer to avoid this complexity. We selected two initial

conditions with better performance for the global vorticity maximum and with small number of excited harmonics, which are denoted as  $I_1$  and  $I_2$  in [7] and summarized in Tabs. I and II in Appendix A along with some simulation information. Note that the number of excited harmonics in the initial vorticity affects directly the speed of the simulation, because we need to calculate  $\boldsymbol{\omega}_0(\mathbf{a})$  for a “shifted”  $\mathbf{a}$ -grid at each time step.

In the paper, we mostly focus on the simulation of the initial condition  $I_2$ , where the pancake structure associated with the global vorticity maximum appears early and we observe its evolution for a longer time interval; analogous results for the initial flow  $I_1$  are summarized in Appendix B. For  $I_2$ , the simulation reaches the final time  $t = 7.5$  in the grid  $1458 \times 648 \times 3456$ , with about two orders of magnitude for the ratio of the lateral pancake dimension to its thickness. We compared these results with the direct simulation of the Euler equations (3) performed as described in [7, 13], which ended at  $t = 8.92$  with the final grid  $1944 \times 972 \times 4374$ . The maximal relative point-by-point difference for the vorticity field  $|\boldsymbol{\omega}^{(1)}(\mathbf{x}) - \boldsymbol{\omega}^{(2)}(\mathbf{x})|/|\boldsymbol{\omega}^{(1)}(\mathbf{x})|$  between the two simulations is kept below  $10^{-9}$  before the grid of the VLR simulation is fixed at  $t = 5.39$ . For larger times, this difference increases up to  $2.1 \times 10^{-8}$  at  $t = 6$  and  $3 \times 10^{-6}$  at  $t = 7$ , and finally reaches  $3 \times 10^{-5}$  at the final time  $t = 7.5$ . This provides independent verification for the accuracy of both numerical schemes.

#### IV. HIGH-VORTICITY AND LOW-JACOBIAN STRUCTURES

For generic initial conditions, the regions of high vorticity developing in 3D incompressible Euler equations have the form of exponentially compressing pancake-like structures [3, 7] with the vorticity vector approximately parallel to the pancake mid-plane. In this section, we study these structures both in the original Eulerian coordinates  $\mathbf{x}$  and in the VLR Lagrangian coordinates  $\mathbf{a}$ .

In the direct simulation of the Euler equations (3), which we performed as described in [7, 13] with the  $I_2$  initial flow, the global vorticity maximum  $\omega_{\max}(t) = \max_{\mathbf{x}} |\boldsymbol{\omega}(\mathbf{x}, t)|$  increases from its initial value  $\omega_{\max}(0) = 1.47$  to 11.2 at  $t = 8.92$ , demonstrating nearly exponential growth  $\omega_{\max}(t) \propto e^{\beta_2 t}$  with  $\beta_2 \approx 0.35$  for  $t \geq 3.5$ , see Fig. 1(a). The region of high vorticity becomes very thin at late times, as shown Fig. 1(c). The figure uses the rotated coordinate axes aligned with the pancake geometry; the explicit definition of these coordinates is given at the end of this Section. The three characteristic sizes of the pancake

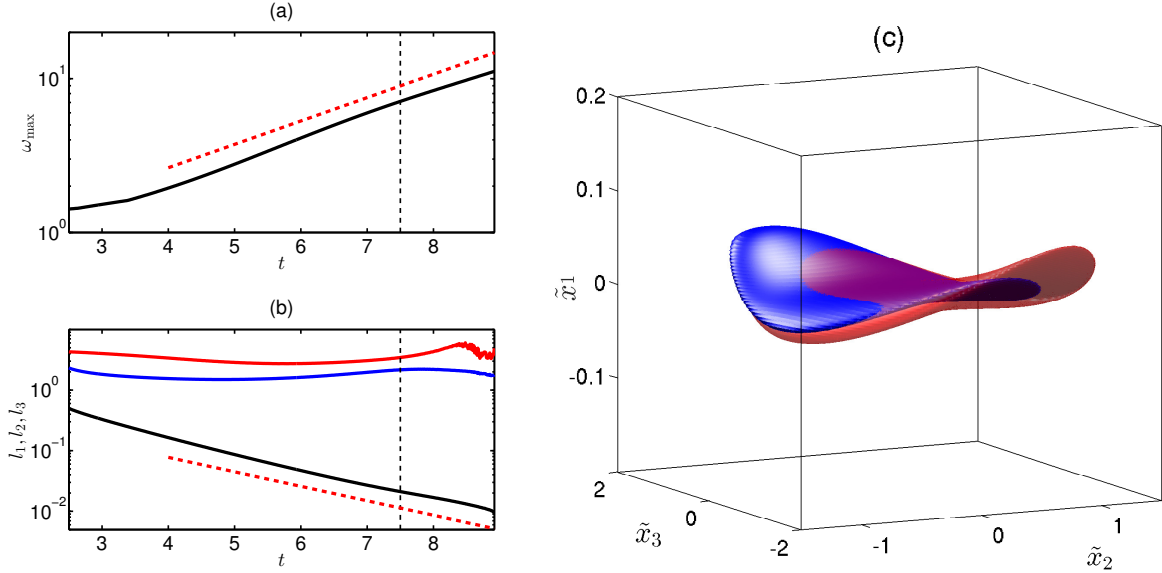


FIG. 1: (*Color on-line*) (a) Global vorticity maximum as a function of time (logarithmic vertical scale) for the direct simulation of the Euler equations (3). The red dashed line indicates the slope  $\propto e^{\beta_2 t}$  with  $\beta_2 = 0.35$ . The vertical dashed line marks the final time  $t = 7.5$  for the simulation of the VLR equations (9)–(11). (b) Time-evolution of the characteristic spatial scales  $l_1$  (black),  $l_2$  (blue) and  $l_3$  (red) for the respective pancake vorticity structure. The red dashed line indicates the slope  $\propto e^{-\beta_1 t}$  with  $\beta_1 = 0.55$ . (c) Isosurfaces of vorticity  $|\boldsymbol{\omega}| = 0.8\omega_{\max}$  (transparent red) and of Jacobian  $J = 1.25 J_{\min}$  (blue) in local  $\tilde{\mathbf{x}}$ -coordinates at the time  $t = 7.1$  of the VLR simulation. Notice a much smaller vertical scale.

can be estimated with the local second-order approximation as  $l_i = \sqrt{2\omega_{\max}/|\lambda_i^\omega|}$ , see [7], where  $|\lambda_1^\omega| \geq |\lambda_2^\omega| \geq |\lambda_3^\omega|$  are the three eigenvalues of the Hessian matrix  $[\partial^2|\boldsymbol{\omega}|/\partial x_i\partial x_j]$ , computed at the point of maximum vorticity  $\omega_{\max}$ ; the location of the maximum in between the grid nodes is approximated with the second-order finite-difference scheme. As illustrated in Fig. 1(b), the smallest size (thickness)  $l_1$  decreases nearly exponentially with time and the other two scales  $l_2$  and  $l_3$  do not change substantially,

$$l_1 \propto e^{-\beta_1 t}, \quad l_2 \propto 1, \quad l_3 \propto 1, \quad (14)$$

so that at the final time the span-to-thickness ratio reaches  $l_2/l_1 \sim l_3/l_1 \gtrsim 100$ .

As expected from the first relation in (8), the regions of large vorticity  $|\boldsymbol{\omega}|$  should correlate with the regions of small Jacobian  $J$ . This is supported by the numerical simulation of the VLR equations. Fig. 1(c) shows that at late time  $t = 7.1$  the (red) region of large



vorticity around the global vorticity maximum mostly overlaps with the (blue) region of small Jacobian. The low-Jacobian region is associated with the Jacobian minimum  $J_{\min}$ , whose position is close to the vorticity maximum. As shown by the time dependency of  $J_{\min}$  in Fig. 2(a), it is the global minimum of the Jacobian until  $t = 7.1$  and becomes a local minimum for later times due to competition with another local minimum  $J'_{\min}$ . Expression (8) relating the VLR with the vorticity contains the nominator  $\widehat{\mathbf{J}}\boldsymbol{\omega}_0(\mathbf{a})$ ; its norm and the resulting relation between the vorticity and the Jacobian are shown for both minima  $J_{\min}$  and  $J'_{\min}$  in Fig. 2(b,c). We see that  $J'_{\min}$  represents a “parasitic” minimum, when both the nominator and denominator decrease sharply, with no increase of the vorticity. Such a behavior is the result of alignment of the vector  $\boldsymbol{\omega}_0$  with the eigenvector corresponding to small eigenvalue of the Jacobi matrix  $\widehat{\mathbf{J}}$ ; the angle between the two decreases to  $14^\circ$  at the final time. We will disregard this parasitic minimum from now on, and focus on the study of the minimum  $J_{\min}$ .

Figure 2(a) shows that time dependency of the Jacobian minimum is close to exponential at late times,  $J_{\min} \propto e^{-\beta_2 t}$ . This behavior is observed in approximately the same time interval and with the same exponent  $\beta_2 = 0.35$  as for the vorticity maximum in Fig. 1(a). The latter leads to inverse proportional relation

$$\omega_{\max}(t) \propto \frac{1}{J_{\min}(t)} \quad (15)$$

between the vorticity maximum and the Jacobian minimum. Recalling the original exact relation (8), we conclude that the growth of the vorticity is related to the smallness of the Jacobian in the denominator, while the nominator plays a secondary role, as was suggested earlier in [16–18]; see Fig. 2(b). We should note that the points of maximum vorticity and minimum Jacobian belong to the same pancake structure and stay close, but may not approach each other with time, as the distance between them decreases up to 0.1 at  $t = 5.9$  and then increases to 0.44 at the final time.

Geometry of the low-Jacobian region in  $\mathbf{x}$ -space, see the blue region in Fig. 1(c), can be described with the three characteristic scales  $\ell_i = \sqrt{2J_{\min}/\lambda_i^{(J)}}$  in the same way as for the high-vorticity regions previously in this section. Here  $\lambda_1^{(J)} \geq \lambda_2^{(J)} \geq \lambda_3^{(J)}$  are the eigenvalues of the Hessian matrix  $\boldsymbol{\Gamma}^{(x)} = [\partial^2 J / \partial x_i \partial x_j]$  computed at the Jacobian minimum  $J_{\min}$ . These eigenvalues correspond to three orthonormal eigenvectors  $\mathbf{n}_1$ ,  $\mathbf{n}_2$  and  $\mathbf{n}_3$ , defining the local coordinate system  $\tilde{\mathbf{x}} = \mathbf{n}_1 \tilde{x}_1 + \mathbf{n}_2 \tilde{x}_2 + \mathbf{n}_3 \tilde{x}_3$  of the pancake used in Fig. 1(c). The three scales

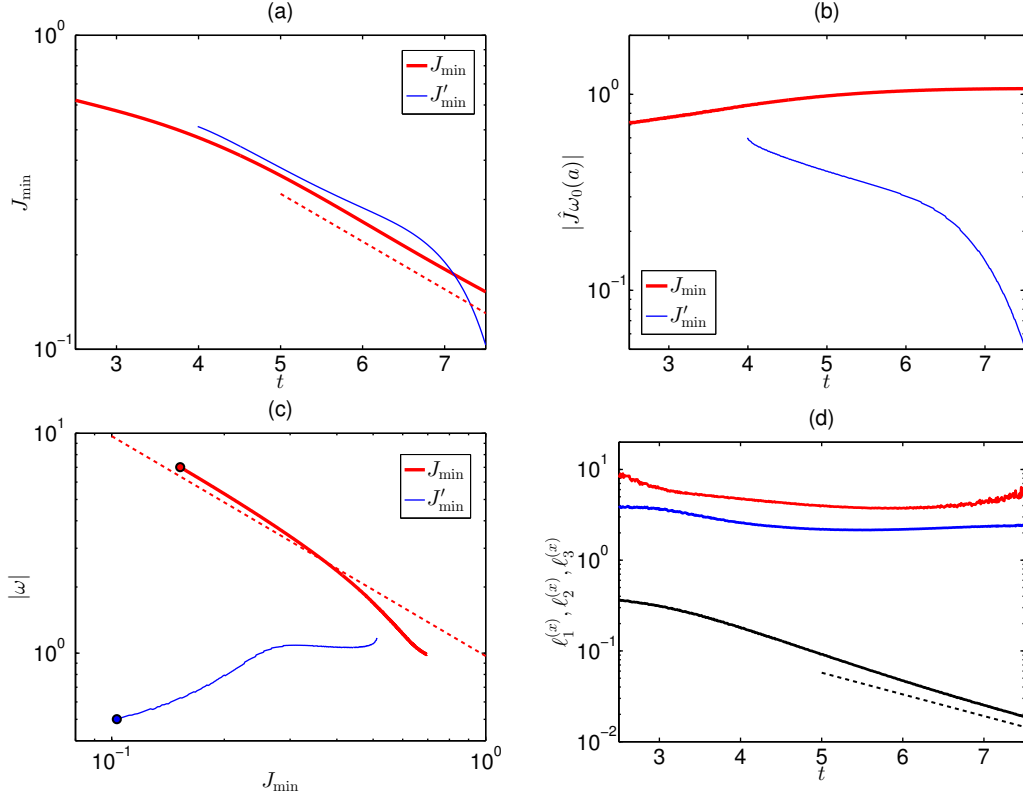


FIG. 2: (*Color on-line*) (a) Time evolution of the two local Jacobian minima. The thick red curve represents the minimum  $J_{\min}$  closest to the global vorticity maximum, and the thin blue curve corresponds to the “parasitic” minimum  $J'_{\min}$ . The red dashed line indicates the slope  $\propto e^{-\beta_2 t}$  with  $\beta_2 = 0.35$ . (b) Norms of the nominator  $\hat{\mathbf{J}}\omega_0(\mathbf{a})$  from Eq. (8) at the same points. (c) Relation between the vorticity and the Jacobian at the same points. The red dashed line indicates the asymptotic relation  $\omega \propto 1/J_{\min}$ , while the circles mark the final time  $t = 7.5$ . (d) Time-evolution of the characteristic spatial scales  $\ell_1$  (black),  $\ell_2$  (blue) and  $\ell_3$  (red) for the low-Jacobian structure corresponding to the minimum  $J_{\min}$ . The black dashed line indicates the slope  $\propto e^{-\beta_1 t}$  with  $\beta_1 = 0.55$ .

$\ell_i$  demonstrate the similar dynamics to that of the high-vorticity region, as can be seen from comparison of Fig. 2(d) and Fig. 1(b), i.e.,

$$\ell_1 \propto e^{-\beta_1 t}, \quad \ell_2 \propto 1, \quad \ell_3 \propto 1. \quad (16)$$

Here the smallest scale  $\ell_1$  (thickness) decreases nearly exponentially with approximately the same exponent  $\beta_1 = 0.55$  as for the vorticity pancake thickness,  $\ell_1 \propto l_1$ , while the other two scales do not change substantially.

Note that, as we define the VLR trajectories with the initial conditions (7), the transformation  $\mathbf{x} = \mathbf{R}\tilde{\mathbf{x}} + \mathbf{x}_m$  to the local coordinate system of the pancake, where  $\mathbf{R} = \{\mathbf{n}_1, \mathbf{n}_2, \mathbf{n}_3\}$  is the rotation matrix and  $\mathbf{x}_m$  is the location of the vorticity maximum, leads to the corresponding transformation  $\mathbf{a} = \mathbf{R}\tilde{\mathbf{a}} + \mathbf{a}_m$ ,  $\mathbf{a}_m = \mathbf{x}_m$ , for the  $\mathbf{a}$ -variables. Hence, the Jacobi matrix  $\tilde{\mathbf{J}} = [\partial\tilde{x}_i/\partial\tilde{a}_j]$  in the pancake coordinate system is related with the Jacobi matrix  $\mathbf{J} = [\partial x_i/\partial a_j]$  in the original system as  $\tilde{\mathbf{J}} = \mathbf{R}^{-1}\mathbf{J}\mathbf{R}$ . All the results below are given for the rotated coordinate systems  $\tilde{\mathbf{x}}$  and  $\tilde{\mathbf{a}}$ ; we will omit the tildes for simplicity.

## V. VLR REPRESENTATION FOR PANCAKE MODEL SOLUTION

Let us test the relation (15) observed numerically in the previous section with a local model for the pancake vorticity structure proposed in [13]. This model represents an exact self-similar solution of the Euler equations (3)

$$\mathbf{v}(\mathbf{x}, t) = -\omega_{\max}(t) l_1(t) f\left(\frac{x_1}{l_1(t)}\right) \mathbf{n}_3 + \begin{pmatrix} -\beta_1 x_1 \\ \beta_2 x_2 \\ \beta_3 x_3 \end{pmatrix}, \quad (17)$$

$$\boldsymbol{\omega}(\mathbf{x}, t) = \omega_{\max}(t) f'\left(\frac{x_1}{l_1(t)}\right) \mathbf{n}_2, \quad (18)$$

written in Cartesian coordinates  $\mathbf{x} = x_1\mathbf{n}_1 + x_2\mathbf{n}_2 + x_3\mathbf{n}_3$  with positive constants  $\beta_1, \beta_2$  and  $\beta_3$  such that  $-\beta_1 + \beta_2 + \beta_3 = 0$ . Here

$$\omega_{\max}(t) = w_0 e^{\beta_2 t}, \quad l_1(t) = h_0 e^{-\beta_1 t}, \quad (19)$$

are the time dependencies for the vorticity maximum and the pancake thickness,  $w_0$  and  $h_0$  are positive prefactors and  $f(\xi)$  is an arbitrary smooth function with  $|\max f'(\xi)| = 1$ . The model (17)-(19) describes a pancake of thickness  $l_1$  oriented perpendicular to  $x_1$ -axis with the vorticity parallel to  $x_2$ -axis. Note that the numerical values of the exponents in our simulation are  $\beta_1 = 0.55$ ,  $\beta_2 = 0.35$  and  $\beta_3 = 0.2$ .

To construct the VLR, we calculate from (17)-(18) the velocity component normal to vorticity,

$$\mathbf{v}_n(\mathbf{x}, t) = -\omega_{\max}(t) l_1(t) f\left(\frac{x_1}{l_1(t)}\right) \mathbf{n}_3 + \begin{pmatrix} -\beta_1 x_1 \\ 0 \\ \beta_3 x_3 \end{pmatrix}. \quad (20)$$

Then we solve (6) with initial conditions (7) and find the VLR mapping

$$x_1 = a_1 e^{-\beta_1 t}, \quad x_2 = a_2, \quad x_3 = a_3 e^{\beta_3 t} - w_0 h_0 f \left( \frac{a_1}{h_0} \right) \frac{\sinh(\beta_3 t)}{\beta_3}, \quad (21)$$

where we used relation  $\beta_1 = \beta_2 + \beta_3$ . The corresponding Jacobi matrix and its determinant become

$$\widehat{\mathbf{J}}(\mathbf{a}, t) = \left[ \frac{\partial x_i}{\partial a_j} \right] = \begin{pmatrix} e^{-\beta_1 t} & 0 & 0 \\ 0 & 1 & 0 \\ -w_0 f' \left( \frac{a_1}{h_0} \right) \frac{\sinh(\beta_3 t)}{\beta_3} & 0 & e^{\beta_3 t} \end{pmatrix}, \quad J = \det \widehat{\mathbf{J}} = e^{(\beta_3 - \beta_1)t} = e^{-\beta_2 t}, \quad (22)$$

and one can verify that expressions (18), (21) and (22) satisfy the equation (8).

As follows from (22), the Jacobian  $J = e^{-\beta_2 t}$  is inverse-proportional to the maximum vorticity  $\omega_{\max}$  from (19), in agreement with the relation (15) and the graph in Fig. 2(b). Note, however, that the Jacobian in (22) does not depend on spatial coordinates, while in simulations it changes sharply along the pancake perpendicular direction, see Fig. 1(c). In the next Section we will show that this sharp dependency in  $\mathbf{x}$ -space comes from small but finite second derivatives of the Jacobian in  $\mathbf{a}$ -space.

## VI. PROPERTIES OF THE VLR MAPPING

As we have demonstrated, high vorticity is related to the decrease of the Jacobian, and therefore the pancake vorticity structures should have a footprint in the VLR mapping  $\mathbf{x} = \mathbf{x}(\mathbf{a}, t)$ . We can study the properties of the mapping using the singular-value decomposition (SVD) of the Jacobi matrix  $\widehat{\mathbf{J}} = [\partial x_i / \partial a_j]$  evaluated at the point of  $J_{\min}$ . The SVD represents transformation  $\widehat{\mathbf{J}} = \mathbf{U} \mathbf{\Sigma} \mathbf{V}^T$  to a diagonal form  $\mathbf{\Sigma} = \text{diag}\{\sigma_1, \sigma_2, \sigma_3\}$  containing real non-negative elements  $0 < \sigma_1 < \sigma_2 < \sigma_3$  called the singular values. Here  $\mathbf{U}$  and  $\mathbf{V}$  are real orthogonal matrices defining rotations in the  $\mathbf{x}$ - and  $\mathbf{a}$ -spaces respectively and  $T$  stands for the matrix transpose. Thus, in the local bases induced by  $\mathbf{U}$  and  $\mathbf{V}$ , the VLR mapping represents a stretching or compression along three orthogonal axes with the rates defined by the singular values  $\sigma_1$ ,  $\sigma_2$  and  $\sigma_3$ .

The time dependency of the singular values, see Fig. 3(a), shows that the VLR mapping near the Jacobian minimum (and, therefore, in the high-vorticity pancake) is strongly compressed along one direction,  $\sigma_1 \ll 1$ , and stretched along the other direction,  $\sigma_3 \gg 1$ . The remaining singular value  $\sigma_2$  is close to unity and does not change with time significantly.

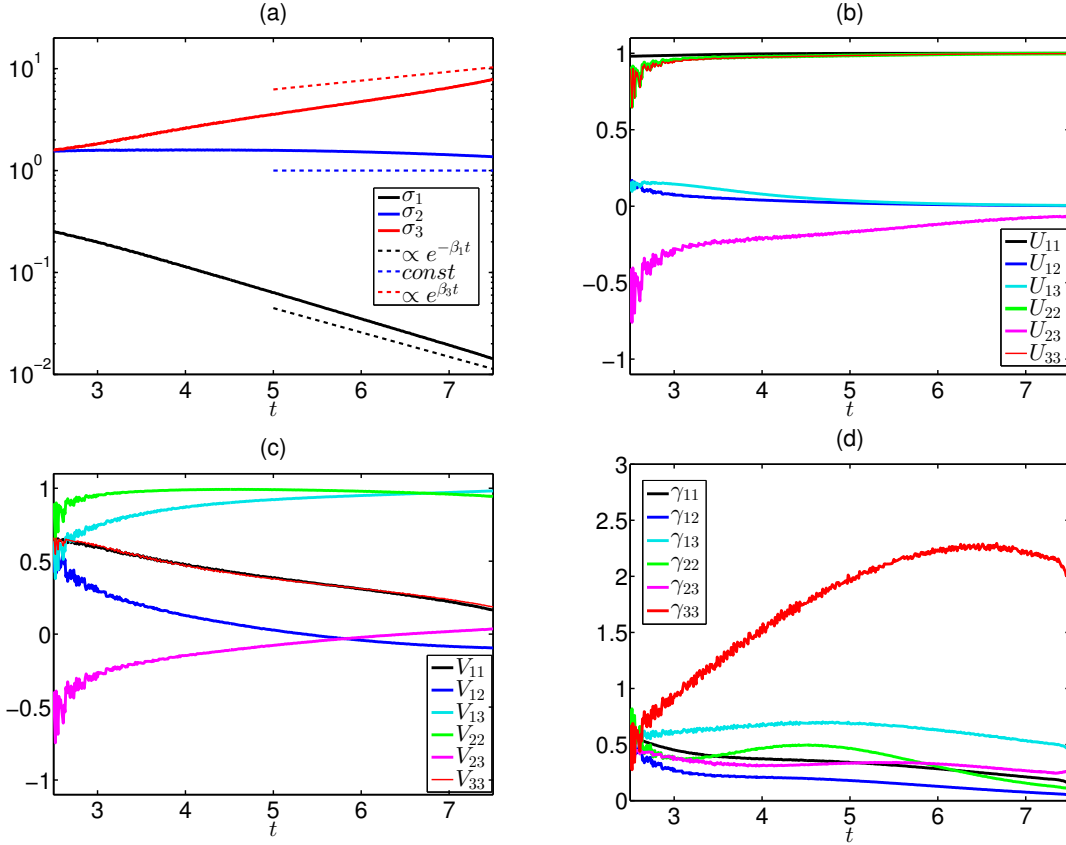


FIG. 3: (*Color on-line*) (a) Singular values  $\sigma_1$  (black),  $\sigma_2$  (blue) and  $\sigma_3$  (red) of the Jacobi matrix  $\widehat{\mathbf{J}}$  computed at  $J_{\min}$ , as functions of time. Dashed lines show the exponential slopes (25). (b) Six components of the rotation matrix  $\mathbf{U}$  in  $\mathbf{x}$ -space, as functions of time. (c) Same for the rotation matrix  $\mathbf{V}$  in  $\mathbf{a}$ -space. (d) Evolution of the Hessian  $\gamma = \mathbf{V}^T \mathbf{\Gamma}^{(a)} \mathbf{V}$  in  $\widehat{V}$ -basis.

This behavior can be explained with the pancake model of Section V, where the VLR mapping and the Jacobi matrix are given explicitly by Eqs. (21), (22). The singular values can be computed as square roots of eigenvalues of the symmetric matrix  $\widehat{\mathbf{J}}\widehat{\mathbf{J}}^T$ , what yields

$$\sigma_1^2 = g - \sqrt{g^2 - e^{-2\beta_2 t}}, \quad \sigma_2^2 = 1, \quad \sigma_3^2 = g + \sqrt{g^2 - e^{-2\beta_2 t}}, \quad (23)$$

where

$$g = \frac{1}{2} \left( e^{-2\beta_1 t} + e^{2\beta_3 t} + \left[ w_0 f' \left( \frac{a_1}{h_0} \right) \frac{\sinh(\beta_3 t)}{\beta_3} \right]^2 \right). \quad (24)$$

The leading terms in the large-time asymptotic of (23) have the form

$$\sigma_1 \propto e^{-\beta_1 t}, \quad \sigma_2 = 1, \quad \sigma_3 \propto e^{\beta_3 t}, \quad (25)$$

what agrees reasonably well with the numerical results in Fig. 3(a), where the exponents are presented by the dashed lines.

The rotation matrices of the SVD provide the orthonormal bases  $\mathbf{U} = \{\mathbf{n}_1^{(x)}, \mathbf{n}_2^{(x)}, \mathbf{n}_3^{(x)}\}$  and  $\mathbf{V} = \{\mathbf{n}_1^{(a)}, \mathbf{n}_2^{(a)}, \mathbf{n}_3^{(a)}\}$  in the  $\mathbf{x}$ - and  $\mathbf{a}$ -spaces, and can be computed as eigenvectors of the symmetric matrices  $\widehat{\mathbf{J}}\widehat{\mathbf{J}}^T$  and  $\widehat{\mathbf{J}}^T\widehat{\mathbf{J}}$ , respectively. For the leading terms in the large-time asymptotic of  $\mathbf{U}$  and  $\mathbf{V}$ , the latter calculation yields

$$\mathbf{U} \propto \mathbf{1}, \quad \mathbf{V} \propto \begin{pmatrix} \frac{1}{\sqrt{1+q^2}} & 0 & \frac{q}{\sqrt{1+q^2}} \\ 0 & 1 & 0 \\ \frac{-q}{\sqrt{1+q^2}} & 0 & \frac{1}{\sqrt{1+q^2}} \end{pmatrix}, \quad (26)$$

where

$$q = -\frac{w_0}{2\beta_3} f' \left( \frac{a_1}{h_0} \right). \quad (27)$$

This is supported by our numerical results, see Fig. 3(b,c): at late times both matrices do not change substantially with  $\mathbf{U}$  close to unity and  $\mathbf{V}$  close to anti-diagonal matrix with elements  $V_{13} \approx V_{22} \approx 1$  and  $V_{23} \approx -1$  (what corresponds to  $q \gg 1$  in Eq. (26)).

The bases  $\mathbf{U}$  and  $\mathbf{V}$  are connected through the Jacobi matrix as  $\widehat{\mathbf{J}}\mathbf{n}_j^{(a)} = \sigma_j \mathbf{n}_j^{(x)}$ ,  $j = 1, 2, 3$ . Thus, as a result of the VLR mapping  $\mathbf{x} = \mathbf{x}(\mathbf{a}, t)$ , the direction  $\mathbf{n}_1^{(a)}$  transforms into  $\mathbf{n}_1^{(x)}$  and undergoes the largest contraction proportional to the pancake thickness  $\sigma_1 \propto e^{-\beta_1 t} = l_1(t)$ , while the direction  $\mathbf{n}_3^{(a)}$  turns into  $\mathbf{n}_3^{(x)}$  and stretches by the factor  $\sigma_3 \propto e^{\beta_3 t}$ . Assuming that such behavior persists in the limit  $t \rightarrow \infty$ , the Lagrangian markers  $\mathbf{a}$  distributed initially along the direction  $\mathbf{n}_1^{(a)}$  collapse to a point. This may be seen as touching of the corresponding vortex lines, with the vorticity growing unboundly  $\omega_{\max}(t) \rightarrow \infty$ .

The sharp dependency of the Jacobian along the pancake perpendicular direction  $x_1$ , see Fig. 1(c), can be explained by finite second derivatives of the Jacobian in  $\mathbf{a}$ -space. At the Jacobian minimum, the Hessian matrices  $\widehat{\Gamma}^{(x)} = [\partial^2 J / \partial x_i \partial x_j]$  and  $\widehat{\Gamma}^{(a)} = [\partial^2 J / \partial a_i \partial a_j]$  are connected by the chain rule

$$\mathbf{\Gamma}^{(a)} = \widehat{\mathbf{J}}^T \mathbf{\Gamma}^{(x)} \widehat{\mathbf{J}}. \quad (28)$$

Substituting the SVD relation  $\widehat{\mathbf{J}} = \mathbf{U}\mathbf{\Sigma}\mathbf{V}^T$  and using the orthogonality of the matrix  $\mathbf{V}$ , we obtain

$$\boldsymbol{\gamma} = \mathbf{V}^T \mathbf{\Gamma}^{(a)} \mathbf{V} = \mathbf{\Sigma} \mathbf{U}^T \mathbf{\Gamma}^{(x)} \mathbf{U} \mathbf{\Sigma}, \quad (29)$$

where  $\boldsymbol{\gamma}$  is the Hessian in  $\mathbf{V}$ -basis. Since in the pancake coordinate system, see Section IV,  $\mathbf{\Gamma}^{(x)}$  is diagonal and  $\mathbf{U}$  is close to unity, the Hessian  $\boldsymbol{\gamma}$  must be close to a diagonal matrix

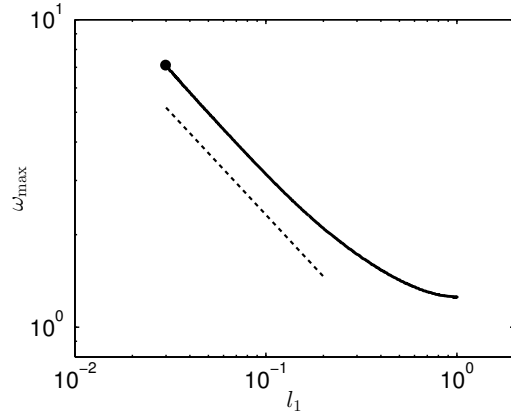


FIG. 4: The vorticity maximum  $\omega_{\max}$  vs. the pancake thickness  $l_1$  in logarithmic scales during the pancake evolution. The circle marks the vorticity maximum at the final time  $t = 7.5$  and the dashed line indicates the power-law  $\omega_{\max} \propto l_1^{-2/3}$ .

too. This agrees with the numerical simulation, see Fig. 3(d), where at late times  $\gamma$  has only the (3,3)-component which is of unity order and does not change significantly, while the other components are small. As  $\mathbf{U}$  is close to unity, the relation (29) yields

$$\gamma_{ii} \approx \sigma_i^2 \lambda_i^{(J)}, \quad i = 1, 2, 3, \quad (30)$$

where  $\lambda_i^{(J)}$  are the eigenvalues of the Hessian  $\mathbf{\Gamma}^{(x)}$ . Then, expanding in the  $\mathbf{x}$ -space the Jacobian near its minimum, we get

$$J - J_{\min} \approx \frac{1}{2} \sum_{i=1}^3 \lambda_i^{(J)} \Delta x_i^2 \approx \frac{1}{2} \sum_{i=1}^3 \gamma_{ii} \left( \frac{\Delta x_i}{\sigma_i} \right)^2. \quad (31)$$

Since only the first singular value of the Jacobi matrix is small and exponentially decreases with time,  $\sigma_1 \propto l_1 \propto e^{-\beta_1 t}$ , all terms except the one proportional to  $\Delta x_1^2$  can be neglected, so that

$$J - J_{\min} \approx \frac{\gamma_{11}}{2} \left( \frac{\Delta x_1}{\sigma_1} \right)^2 \propto \gamma_{11} \left( \frac{\Delta x_1}{l_1} \right)^2. \quad (32)$$

Hence, the sharp dependency of the Jacobian in  $x_1$ -direction comes from small but finite component  $\gamma_{11}$ .

The eigenvalues of the Hessian  $\mathbf{\Gamma}^{(x)}$  are connected with the characteristic scales of the low-Jacobian structure,  $\lambda_i^{(J)} = 2J_{\min}/\ell_i^2$ , and the relation (30) can be rewritten as

$$\gamma_{ii} \approx 2J_{\min} \sigma_i^2 / \ell_i^2, \quad i = 1, 2, 3. \quad (33)$$

Since  $\sigma_1 \propto \ell_1 \propto l_1$  and  $\sigma_2 \sim \ell_2 \sim 1$ , see Eqs. (14), (16), (25), the components  $\gamma_{11}$  and  $\gamma_{22}$  should decay as the Jacobian,  $J_{\min} \propto e^{-\beta_2 t}$ . As shown in Fig. 3(d), these components indeed decay, however they do not follow the mentioned dependency exactly, what may be connected with the difference between  $\mathbf{U}$  and the unity matrix. For the large (3, 3)-component we have  $\ell_3 \sim 1$  and  $\sigma_3 \propto e^{\beta_3 t} \propto \omega_{\max}^{-1} \ell_1^{-1}$ , so that

$$\gamma_{33} \approx 2J_{\min} \sigma_3^2 / \ell_3^2 \propto J_{\min} \omega_{\max}^{-2} l_1^{-2} \propto \omega_{\max}^{-3} l_1^{-2}, \quad (34)$$

where we used the inverse-proportionality between the vorticity maximum and the Jacobian minimum (15). Hence, when the (3, 3)-component does not depend on time significantly, see Fig. 3(d), the relation (34) leads to the 2/3-scaling  $\omega_{\max} \propto l_1^{-2/3}$  between the vorticity maximum and the pancake thickness during the pancake evolution, as confirmed by the numerical simulation in Fig. 4.

The results discussed above are related to the high-vorticity structure corresponding to the global vorticity maximum and are obtained from the simulation of the initial condition  $I_2$ . We verified that several other pancakes from the same simulation corresponding to other local maxima of vorticity, as well as pancakes from the simulation for the initial flow  $I_1$ , discussed in Appendix B, demonstrate the same properties for the Jacobi and the Hessian matrices.

## VII. CONCLUSION

In this paper we have studied high-vorticity regions developing in the incompressible 3D Euler equations from the point of view of the VLR. The VLR is the transition from the Eulerian coordinates of the flow to the Lagrangian markers of the vortex lines, which is compressible, so that its Jacobian may take arbitrary values. The vorticity of the flow is expressed through the Jacobi matrix of the VLR (8), and, in the general case, it should grow when the Jacobian decreases. Led by this observation, we developed a numerical method for the Euler equations in terms of the VLR and performed high-resolution simulations for two initial flows.

For generic initial conditions, the regions of high vorticity have the form of the pancake-like structures (thin vorticity sheets) with exponentially decreasing thickness  $l_1 \propto e^{-\beta_1 t}$  and growing vorticity  $\omega_{\max} \propto e^{\beta_2 t}$ . The ratio between the exponents  $\beta_2/\beta_1 \approx 2/3$  leads



to the 2/3-scaling law (1) between the vorticity maximum and the pancake thickness, as we demonstrated previously in [7]. In the present paper we have shown that the pancake vorticity structures are indeed characterized by the decreased Jacobian, and the inverse-proportional relation between the vorticity maximum and the Jacobian minimum is satisfied,  $\omega_{\max} \propto 1/J_{\min}$ . The pancakes have a footprint on the VLR mapping, which we analyze with the SVD for Jacobi matrix. The singular values show that the mapping is strongly compressed along one direction,  $\sigma_1 \propto l_1 \propto e^{-\beta_1 t}$ , stretched along the other one,  $\sigma_3 \propto \omega_{\max}^{-1} l_1^{-1} \propto e^{\beta_3 t}$ , while the third singular value does not change with time substantially,  $\sigma_3 \propto 1$ . These results also follow analytically from the VLR written for the pancake model solution of [13]. The rotation matrices  $\mathbf{U}$  and  $\mathbf{V}$  of the SVD diagonalize the Hessian matrices of the Jacobian  $\mathbf{\Gamma}^{(x)}$  and  $\boldsymbol{\gamma}$ , in  $\mathbf{x}$ - and  $\mathbf{a}$ -spaces respectively. The analysis of the Hessians show, that the 2/3-scaling law is linked with the finite lateral size of the low-Jacobian pancake,  $l_3 \propto 1$ , and finite element of the Hessian  $\gamma_{33} \propto 1$ . The sharp dependency of the Jacobian along the pancake perpendicular direction, on the other hand, comes from small but finite element  $\gamma_{11}$ .

The finiteness of the Hessian elements  $\gamma_{ij}$  does not follow from the pancake model solution, for which the Jacobian does not depend on spatial coordinates (22) and  $\boldsymbol{\gamma} = \mathbf{0}$ . However, in simulations the pancake vorticity structures are not completely flat, with deviations from a pure plane much larger than the pancake thickness, see e.g. Fig. 1(c). This means that the model (17)-(18) cannot describe the whole pancake structure. On the other hand, as we demonstrated in [13], this model describes locally an every nearly flat pancake segment with the model parameters changing significantly from one segment to another. We think that this behavior comes from nonlocal effects and may result in finite Jacobian second derivatives in  $\mathbf{a}$ -space, as observed in Fig. 3(d).

We should note that our approach utilizes general properties of the frozen-in-fluid fields and, potentially, can be generalized to a wide group of physical phenomena far beyond the scope of this paper. For instance, compressibility of magnetic field lines [19] should play an essential role in generation of magnetic filaments in the convective zone of the Sun and in the magnetic dynamo theories in space plasma, see e.g. [24, 25]. As shown in [20, 26, 27], compressible character of the frozen-in-fluid divorticity field is an important factor in the formation of direct Kraichnan cascade in 2D hydrodynamic turbulence, and thereby it may be crucial in understanding of large-scale structures in planetary atmospheres.

### Acknowledgements

Development of the numerical code and simulations were supported by the RFFI grant 17-01-00622, with the latter performed at the Novosibirsk Supercomputer Center (NSU). Analysis of the results was done at the Data Center of IMPA (Rio de Janeiro). D.S.A. acknowledges the support from IMPA during the visits to Brazil. A.A.M. was supported by the CNPq (grant 302351/2015-9) and the Program FAPERJ Pensa Rio (grant E-26/210.874/2014).

- 
- [1] D. Chae, *Incompressible Euler Equations: the blow-up problem and related results*. In: *Handbook of Differential Equations: Evolutionary Equation (C.M. Dafermos and M. Pokorný, Eds.), Vol. 4*, pp. 1–55. Elsevier, 2008.
  - [2] J. D. Gibbon, “The three-dimensional Euler equations: Where do we stand?,” *Physica D*, vol. 237, no. 14-17, pp. 1894–1904, 2008.
  - [3] M. E. Brachet, M. Meneguzzi, A. Vincent, H. Politano, and P. L. Sulem, “Numerical evidence of smooth self-similar dynamics and possibility of subsequent collapse for three-dimensional ideal flows,” *Phys. Fluids A*, vol. 4, pp. 2845–2854, 1992.
  - [4] A. J. Majda and A. L. Bertozzi, *Vorticity and incompressible flow*. Cambridge University Press, 2002.
  - [5] A. Pumir and E. Siggia, “Collapsing solutions to the 3-D Euler equations,” *Phys. Fluids A*, vol. 2, pp. 220–241, 1990.
  - [6] K. Ohkitani, “A geometrical study of 3D incompressible Euler flows with Clebsch potentials: a long-lived Euler flow and its power-law energy spectrum,” *Physica D*, vol. 237, no. 14, pp. 2020–2027, 2008.
  - [7] D. S. Agafontsev, E. A. Kuznetsov, and A. A. Mailybaev, “Development of high vorticity structures in incompressible 3D Euler equations,” *Phys. Fluids*, vol. 27, p. 085102, 2015.
  - [8] T. Y. Hou, “Blow-up or no blow-up? A unified computational and analytic approach to 3D incompressible Euler and Navier–Stokes equations,” *Acta Numerica*, vol. 18, pp. 277–346, 2009.
  - [9] M. D. Bustamante and M. Brachet, “Interplay between the Beale-Kato-Majda theorem and the analyticity-strip method to investigate numerically the incompressible Euler singularity

- problem,” *Phys. Rev. E*, vol. 86, no. 6, p. 066302, 2012.
- [10] R. M. Kerr, “Bounds for Euler from vorticity moments and line divergence,” *J. Fluid Mech.*, vol. 729, p. R2, 2013.
- [11] G. Luo and T. Y. Hou, “Potentially singular solutions of the 3D incompressible Euler equations,” *PNAS*, vol. 111, pp. 12968–12973, 2014.
- [12] D. S. Agafontsev, E. A. Kuznetsov, and A. A. Mailybaev, “Development of high vorticity in incompressible 3D Euler equations: influence of initial conditions,” *JETP letters*, vol. 104, no. 10, pp. 775–780, 2016.
- [13] D. S. Agafontsev, E. A. Kuznetsov, and A. A. Mailybaev, “Asymptotic solution for high-vorticity regions in incompressible three-dimensional Euler equations,” *JFM*, vol. 813, p. R1, 2017.
- [14] E. A. Kuznetsov and V. P. Ruban, “Hamiltonian dynamics of vortex lines in hydrodynamic-type systems,” *J. Exp. Theor. Phys. Letters*, vol. 67, no. 12, pp. 1076–1081, 1998.
- [15] S. F. Shandarin and Y. B. Zeldovich, “The large-scale structure of the universe: Turbulence, intermittency, structures in a self-gravitating medium,” *Rev. Mod. Phys.*, vol. 61, no. 2, p. 185, 1989.
- [16] E. A. Kuznetsov and V. P. Ruban, “Collapse of vortex lines in hydrodynamics,” *JETP*, vol. 91, no. 4, pp. 775–785, 2000.
- [17] E. A. Kuznetsov, “Breaking of vortex and magnetic field lines in hydrodynamics and MHD,” *AIP Conf. Proc.*, vol. 703, no. 1, pp. 16–25, 2004.
- [18] E. A. Kuznetsov, “Vortex line representation for the hydrodynamic type equations,” *JNMP*, vol. 13, no. 1, pp. 64–80, 2006.
- [19] E. A. Kuznetsov, T. Passot, and P. L. Sulem, “Compressible dynamics of magnetic field lines for incompressible magnetohydrodynamic flows,” *Phys. Plasmas*, vol. 11, no. 4, pp. 1410–1415, 2004.
- [20] E. A. Kuznetsov, V. Naulin, A. H. Nielsen, and J. J. Rasmussen, “Effects of sharp vorticity gradients in two-dimensional hydrodynamic turbulence,” *Phys. Fluids*, vol. 19, no. 10, p. 105110, 2007.
- [21] E. A. Kuznetsov and V. P. Ruban, “Hamiltonian dynamics of vortex and magnetic lines in hydrodynamic type systems,” *Phys. Rev. E*, vol. 61, no. 1, p. 831, 2000.
- [22] E. A. Kuznetsov, “Mixed Lagrangian–Eulerian description of vortical flows for ideal and vis-

- cous fluids,” *J. Fluid Mech.*, vol. 600, pp. 167–180, 2008.
- [23] T. Y. Hou and R. Li, “Computing nearly singular solutions using pseudo-spectral methods,” *J. Comp. Phys.*, vol. 226, no. 1, pp. 379–397, 2007.
- [24] H. K. Moffatt, *Field Generation in Electrically Conducting Fluids*. Cambridge University Press, 1978.
- [25] S. Childress and A. D. Gilbert, *Stretch, twist, fold: the fast dynamo*, vol. 37. Springer Science & Business Media, 2008.
- [26] A. N. Kudryavtsev, E. A. Kuznetsov, and E. V. Sereshchenko, “Statistical properties of freely decaying two-dimensional hydrodynamic turbulence,” *JETP Lett.*, vol. 96, no. 11, pp. 699–705, 2013.
- [27] E. A. Kuznetsov and E. V. Sereshchenko, “Anisotropic characteristics of the Kraichnan direct cascade in two-dimensional hydrodynamic turbulence,” *JETP Lett.*, vol. 102, no. 11, pp. 760–765, 2015.

### Appendix A: Initial conditions for numerical simulations

We consider initial vorticity at  $t = 0$  in the form of Fourier series

$$\boldsymbol{\omega}_0(\mathbf{x}) = \sum_{\mathbf{h}} [\mathbf{A}_{\mathbf{h}} \cos(\mathbf{h} \cdot \mathbf{x}) + \boldsymbol{\omega}_{\mathbf{h}} \sin(\mathbf{h} \cdot \mathbf{x})], \quad (\text{A1})$$

where  $\mathbf{h} = (h_1, h_2, h_3)$  is a vector with integer components. Due to incompressibility, real vectors  $\mathbf{A}_{\mathbf{h}}$  and  $\boldsymbol{\omega}_{\mathbf{h}}$  must satisfy orthogonality conditions,  $\mathbf{h} \cdot \mathbf{A}_{\mathbf{h}} = \mathbf{h} \cdot \boldsymbol{\omega}_{\mathbf{h}} = 0$ , necessary for self-consistency. The paper is based on two selected initial conditions  $I_1$  and  $I_2$ , for which we provide all nonzero vectors  $\mathbf{A}_{\mathbf{h}}$  and  $\boldsymbol{\omega}_{\mathbf{h}}$  in the Tables below.

TABLE I: Nonzero coefficients in Eq. (A1) for the initial vorticity field  $I_1$  with the average energy density  $E/(2\pi)^3 \approx 0.54$  and the average helicity density  $\Omega/(2\pi)^3 \approx 1.05$ .

$\mathbf{h}$	$\mathbf{A}_{\mathbf{h}}$	$\mathbf{B}_{\mathbf{h}}$
(-1,0,2)	(0.0065641, 0.0027931, 0.003282)	(0.0044136, 0.0056271, 0.0022068)
(0,0,0)	(0.065101, 0.0005801, -0.064109)	(0.0045744, -0.022895, 0.18392)
(0,0,1)	(0, 1, 0)	(1, 0, 0)
(0,0,2)	(0, 0.01, 0)	(0.01, 0, 0)
(0,1,0)	(0.21204, 0, -0.070625)	(-0.14438, 0, 0.23298)
(0,1,1)	(0.045977, -0.010151, 0.010151)	(0.041942, 0.040326, -0.040326)
(0,2,0)	(0.005, 0, 0)	(0, 0, 0.005)
(1,0,0)	(0, 0, 0.1)	(0, 0.1, 0)
(1,0,1)	(-0.046112, 0.017081, 0.046112)	(-0.0097784, 0.020122, 0.0097784)
(1,1,2)	(-0.0034664, 0.0049556, -0.00074462)	(-0.0059316, -0.0010472, 0.0034894)
(2,0,0)	(0, 0, 0.02)	(0, 0.02, 0)

TABLE II: Nonzero coefficients in Eq. (A1) for the initial vorticity field  $I_2$  with the average energy density  $E/(2\pi)^3 \approx 0.55$  and the average helicity density  $\Omega/(2\pi)^3 \approx 1$ .

$\mathbf{h}$	$\mathbf{A}_{\mathbf{h}}$	$\mathbf{B}_{\mathbf{h}}$
(-1,0,1)	(-0.040618, 0.039651, -0.040618)	(-0.030318, 0.064657, -0.030318)
(0,0,0)	(0.067751, -0.1311, -0.11256)	(-0.082614, -0.0364, 0.18932)
(0,0,1)	(0, 1, 0)	(1, 0, 0)
(0,1,1)	(0.0062549, 0.044315, -0.044315)	(0.034983, -0.014521, 0.014521)
(1,0,0)	(0, 0.079395, 0.07027)	(0, 0.099411, 0.012762)
(1,1,0)	(-0.047174, 0.047174, -0.045572)	(-0.049622, 0.049622, 0.001773)

### Appendix B: Simulation results for the $I_1$ initial flow

In this Appendix we provide some results for the simulation of the  $I_1$  initial condition from Tab. I. The direct simulation of the Euler equations (3) for this flow in  $2048^3$  grid is given in [13]. It ends at  $t = 7.75$  with the grid  $972 \times 2048 \times 4096$  and the global vorticity maximum increased from 1.5 at  $t = 0$  to 18.4 at the final time. At late times, the vorticity maximum increases as  $\omega_{\max} \propto e^{\beta_2 t}$  with  $\beta_2 = 0.5$  and the pancake thickness decays as  $l_1 \propto e^{-\beta_1 t}$  with  $\beta_1 = 0.74$ , while the lateral pancake dimensions do not change significantly,  $l_{2,3} \propto 1$ , see Fig. 5(a,b).

The VLR simulation ends at  $t = 5.64$  with the grid  $648 \times 1536 \times 3456$  and the vorticity maximum 6.3 at the final time, as indicated by the vertical line in Fig. 5(a). At late times, the Jacobian minimum close to the global vorticity maximum decays exponentially and inverse-proportionally to the vorticity maximum,  $J_{\min} \propto \omega_{\max}^{-1} \propto e^{-\beta_2 t}$ , see Fig. 5(c). The thickness of the corresponding low-Jacobian region decays as the vorticity pancake thickness,  $l_1 \propto l_1 \propto e^{-\beta_1 t}$ , with the longitudinal scales not changing substantially,  $l_{2,3} \propto 1$ , see Fig. 5(d). The first singular value of the Jacobi matrix computed at  $J_{\min}$  decays as the vorticity pancake thickness,  $\sigma_1 \propto l_1 \propto e^{-\beta_1 t}$ , the second one does not change significantly,  $\sigma_2 \propto 1$ , and the third singular value increases close to exponentially, Fig. 6(a). At late times, the rotation matrices of the SVD do not change substantially with  $\mathbf{U}$  close to unity and  $\mathbf{V}$  close to anti-diagonal matrix with elements  $V_{13} \approx V_{22} \approx 1$  and  $V_{22} \approx -1$ , Fig. 6(b,c). The Hessian in  $\mathbf{V}$ -basis  $\gamma$  is almost diagonal, has only the (3,3)-component of unity order which does not change significantly in time, while the other components are small, Fig. 6(d). Hence, we conclude that the simulation of  $I_1$  initial flow leads to the same conclusions on the formation of intense vorticity due to decay of the Jacobian and the emergence of the 2/3-scaling from the geometric properties of the VLR, as deduced from the  $I_2$  simulation in the main text of this paper.

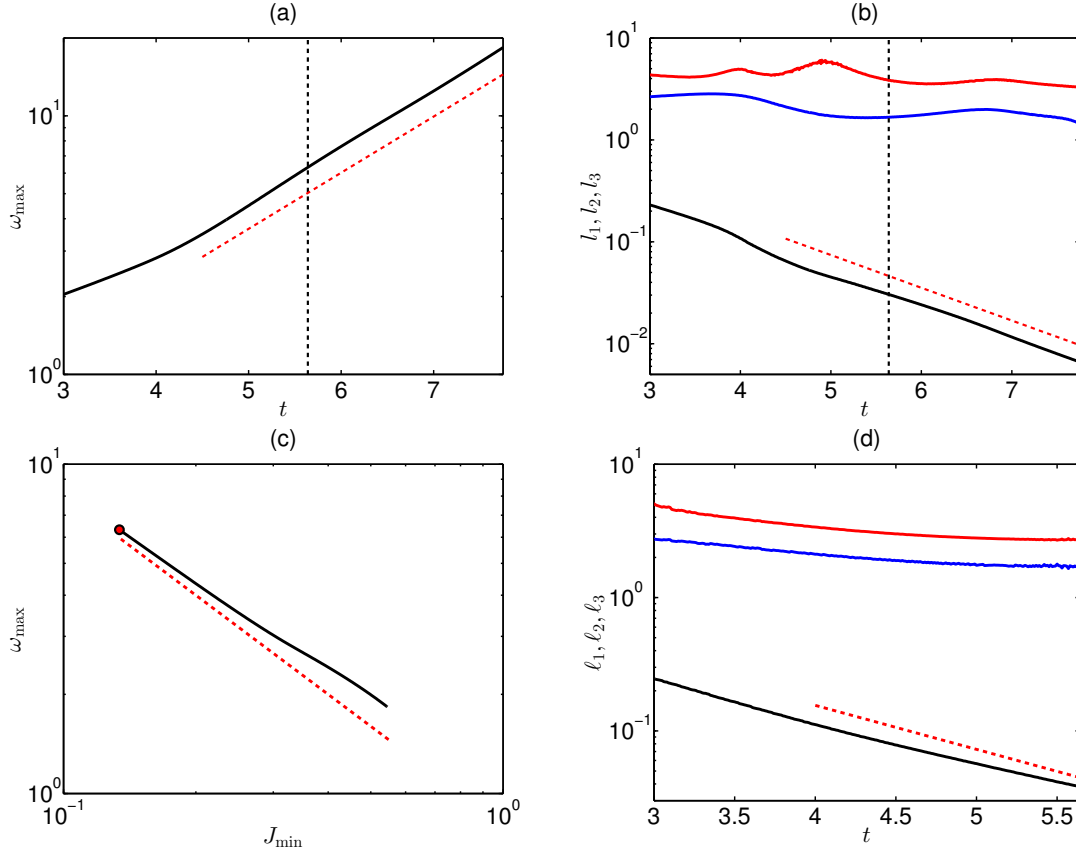


FIG. 5: (*Color on-line*) (a) Global vorticity maximum as a function of time (logarithmic vertical scale) for the direct simulation of the Euler equations (3). The red dashed line indicates the slope  $\propto e^{\beta_2 t}$  with  $\beta_2 = 0.5$ . The vertical dashed line marks the final time  $t = 5.64$  for the simulation of the VLR equations (9)–(11). (b) Time-evolution of the characteristic spatial scales  $l_1$  (black),  $l_2$  (blue) and  $l_3$  (red) for the respective pancake vorticity structure. The red dashed line indicates the slope  $\propto e^{-\beta_1 t}$  with  $\beta_1 = 0.74$ . (c) Relation between the vorticity and the Jacobian at the Jacobian minimum  $J_{\min}$  closest to the global vorticity maximum, the VLR simulation. The red dashed line indicates the asymptotic relation  $\omega \propto 1/J_{\min}$ , while the circle marks the final time  $t = 5.64$ . (d) Time-evolution of the characteristic spatial scales  $\ell_1$  (black),  $\ell_2$  (blue) and  $\ell_3$  (red) for the low-Jacobian structure corresponding to the minimum  $J_{\min}$ . The black dashed line indicates the slope  $\propto e^{-\beta_1 t}$  with  $\beta_1 = 0.74$ .

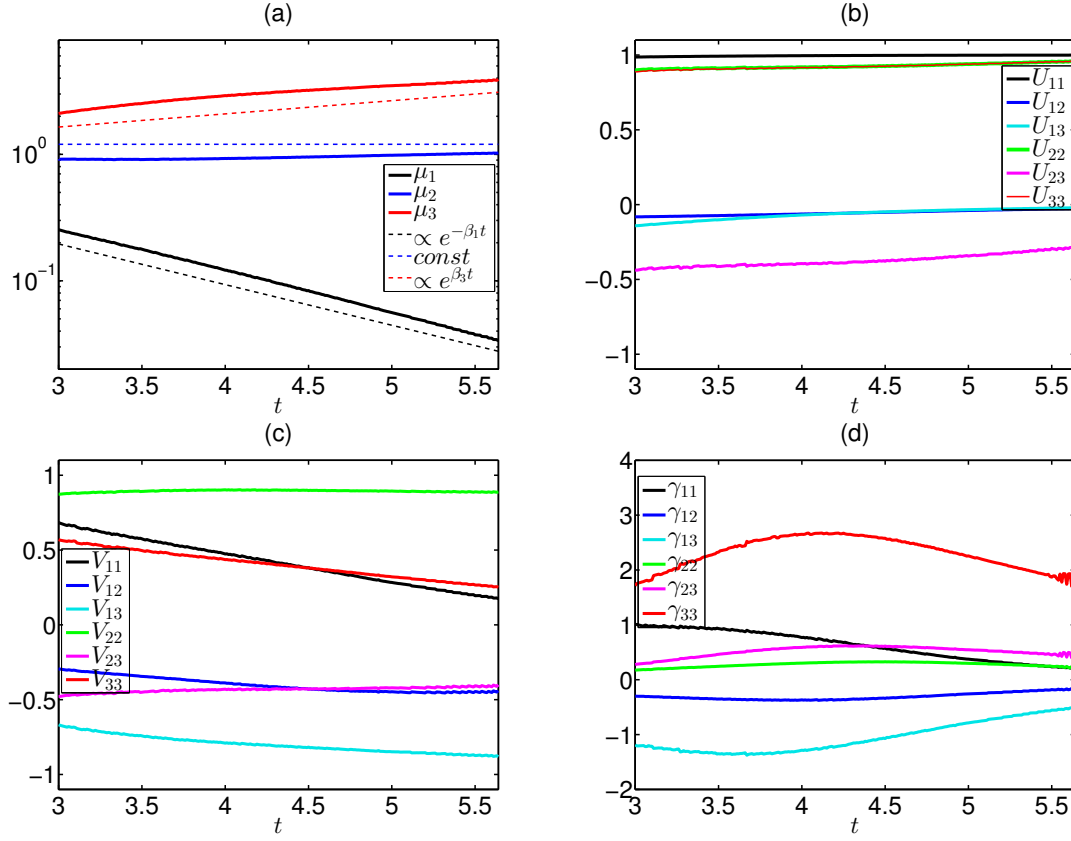


FIG. 6: (*Color on-line*) (a) Singular values  $\sigma_1$  (black),  $\sigma_2$  (blue) and  $\sigma_3$  (red) of the Jacobi matrix  $\hat{\mathbf{J}}$  computed at  $J_{\min}$ , as functions of time. Dashed lines show the exponential slopes (25) with  $\beta_1 = 0.74$ ,  $\beta_2 = 0.5$  and  $\beta_3 = 0.24$ . (b) Six components of the rotation matrix  $\mathbf{U}$  in  $\mathbf{x}$ -space, as functions of time. (c) Same for the rotation matrix  $\mathbf{V}$  in  $\mathbf{a}$ -space. (d) Evolution of the Hessian  $\gamma = \mathbf{V}^T \mathbf{\Gamma}^{(a)} \mathbf{V}$  in  $\hat{V}$ -basis.